

Quantum computing with error mitigation for data-driven computational homogenization

Zengtao Kuang^{a,†}, Yongchun Xu^{a,†}, Qun Huang^a, Jie Yang^a,
Chafik El Kihal^a, Heng Hu^{a,*}

^aSchool of Civil Engineering, Wuhan University, 8 South Road of East Lake, Wuchang, 430072
Wuhan, PR China

Abstract

As a crossover frontier of physics and mechanics, quantum computing is showing its great potential in computational mechanics. However, quantum hardware noise remains a critical barrier to achieving accurate simulation results due to the limitation of the current hardware. In this paper, we integrate error-mitigated quantum computing in data-driven computational homogenization, where the zero-noise extrapolation (ZNE) technique is employed to improve the reliability of quantum computing. Specifically, ZNE is utilized to mitigate the quantum hardware noise in two quantum algorithms for distance calculation, namely a Swap-based algorithm and an H-based algorithm, thereby improving the overall accuracy of data-driven computational homogenization. Numerical examples including a multiscale simulation of a composite L-shaped beam are conducted with the quantum computer simulator Qiskit, and the results validate the effectiveness of the proposed method. We believe this work presents a promising step towards using quantum computing in computational mechanics.

Keywords: Quantum computing; Data-driven computational homogenization; Error mitigation; Zero-noise extrapolation; Distance calculation.

1 Introduction

Due to the unique properties of quantum systems like superposition and entanglement, quantum computing enables exponentially reducing the complexity of computation in certain tasks. It has attracted the increasing attention of researchers in the field of computational mechanics. Until now, quantum computing has been applied to solve, e.g., boundary value problems with finite element method [1], Poisson's equation [2], fluid dynamics [3], composite materials [4], optimization problems [5] and so on. Recently, Xu et al. [6] introduced a quantum computing enhanced data-driven method, which was validated both in a quantum computer simulator and a real quantum computer. However, the noise remains one of the limitations of the current quantum hardware, which prevents taking advantage of quantum computing. In this work, we aim to extend the quantum computing enhanced data-driven method in composite

[†]These authors contributed equally to this work.

^{*}Corresponding author. E-mail address: huheng@whu.edu.cn.

structures, and reduce the error from quantum hardware noise so as to improve the accuracy of quantum computing.

Data-driven computational mechanics is a novel approach to solving boundary value problems (BVP) in the domain of mechanics [7]. In this computing paradigm, the simulation is conducted by using material data directly, therefore bypassing the need for material modeling. Based on this approach, Xu et al. [8] proposed a data-driven computational homogenization method for multiscale simulation of composite structures, where the microscopic problem is solved in advance to generate a material database, which is then utilized for data-driven computing in the macroscopic problem. Compared to the multiscale finite element method [9], it reduces the high computational cost from the correlation between different scales. The data-driven computational homogenization has been rapidly applied in polymer composites [10], fiber reinforced composites [11–16], particle material [17], and so on. The data-driven method relies on iteratively shortening the distance between material data and conservation laws, which requires nearest-neighbor searches in a material database concerning numerous distance calculations. Specifically, if a nearest-neighbor search is performed in a material database with N data, each having dimension D , then N distance calculations are required, each with a cost $O(D)$, leading to a computational complexity of $O(ND)$. When involving a high-dimensional and high-density material database, the distance calculations become a computational bottleneck. For example, for a 3D elastic solid problem with 10^6 material data, the nearest-neighbor search takes more than 90% of the total time [18].

The emergence of the quantum computer shows promise in accelerating distance calculations in data-driven computational homogenization. In the work of Xu et al. [6], a quantum algorithm is introduced to exponentially reduce the complexity of distance calculations from $O(D)$ to $O(\log D)$, therefore improving the overall performance of data-driven computing. However, they assume the usage of a fault-tolerant quantum computer [19, 20], and quantum hardware noise is not considered. In fact, quantum hardware noise can affect the accuracy of quantum algorithms in distance calculations, thereby decreasing the overall precision of data-driven computing. This noise issue is particularly evident in data-driven computational homogenization due to the complex constitutive relationships of composite structures, which require more material data and higher accuracy in distance calculations. The hardware noise in quantum computers usually originates from unexpected interactions with the environment and from imperfect gate operations [21]. For instance, environmental disturbances can lead to decoherence in a quantum system, resulting in the loss of information. Meanwhile, unlike classical bits confined to 0 and 1, quantum bits (qubits) in quantum computers can be any superposition of $|0\rangle$ and $|1\rangle$. This makes quantum computers prone to output inaccurate information even with small disturbance [22]. Therefore, addressing the errors caused by the hardware noise is a crucial issue for the application of quantum computing.

The primary objective of this paper is to address the quantum hardware noise issue, thereby improving the reliability of quantum computing for its practical application in data-driven computational homogenization. Currently, there are two kinds of quantum algorithms that can be considered to achieve the goal [22]. The first is quantum error correction (QEC), which offers

a solution by redundantly encoding quantum information with additional qubits and actively detecting and correcting errors [21, 23], resulting in fault-tolerant computing. Unfortunately, the hardware level of quantum computers is now in the era named Noisy Intermediate-Scale Quantum (NISQ) [24], meaning the number of qubits is limited. However, QEC requires a large overhead number of additional qubits, making it infeasible for NISQ quantum computers [22, 24]. The second approach, quantum error mitigation (QEM), emerges as a more practical alternative for NISQ devices [25]. One prominent QEM method is zero-noise extrapolation (ZNE), which intentionally introduces additional noise and extrapolates results to the zero-noise limit [26, 27]. An advantage of ZNE is its independence from additional qubits, rendering it well-suited for NISQ quantum computers. ZNE has been able to improve the accuracy of a noisy superconducting quantum processor to an inaccessible level [28]. Notably, IBM Quantum recently demonstrated the utility of NISQ quantum computers before the fault-tolerant era with the help of ZNE, which passes a calculation milestone in the field of quantum computing [29, 30].

In this paper, we aim to use quantum computing to reduce the complexity of distance calculation in data-driven computational homogenization, and employ ZNE to mitigate the quantum hardware noise. Two quantum algorithms for distance calculations are presented, i.e., an algorithm based on swap test (Swap-based) [6, 31] and an algorithm based on one Hadamard gate (H-based) [32, 33], and ZNE is employed to improve their accuracy considering quantum hardware noise. Furthermore, a k -d tree data structure [18, 34–36] is used to reduce the number of distance calculations, resulting in a more favorable computational complexity. The quantum computer simulator Qiskit [37] which allows one to execute quantum algorithms on classical computers, is utilized to validate the proposed approach. Several numerical experiments are conducted to confirm the effectiveness of ZNE in improving the accuracy of distance calculation. Moreover, we present a multiscale simulation of a composite L-shaped beam to illustrate the practical utility of the proposed methodology.

The remainder of this article is laid out as follows. In Section 2, we introduce the fundamental formulations of data-driven computational homogenization and the two quantum algorithms for distance calculation. Subsequently, the basic formulation of ZNE for mitigating quantum hardware noise is demonstrated. In Section 3, we present numerical examples to evaluate the performance of the two quantum algorithms considering hardware noise, and validate the effectiveness of ZNE in improving the accuracy of distance calculation. Additionally, we use a roof truss as a case study to emphasize the impact of ZNE on improving the accuracy of data-driven computing. A multiscale simulation of a composite L-shaped beam is presented in Section 4 as an application example, and conclusions are provided in Section 5.

2 Methodology

In Section 2.1, we briefly introduce the formulations of data-driven computational homogenization. This computing scheme involves computationally expensive distance calculations for nearest-neighbor searches. Therefore, the two quantum algorithms for distance calculation are introduced in Section 2.2 to reduce the computational complexity. Finally, the formulation of

ZNE for mitigating the influence of hardware noise is introduced in Section 2.3.

2.1 Data-driven computational homogenization

In the framework of data-driven computational homogenization, the microscopic and macroscopic problems are solved separately [8]. The microscopic problem is solved offline to construct the material database $\bar{\mathcal{D}}$, while the macroscopic problem is solved online to obtain the mechanical response of the structure, in which the material behavior is directly provided by the material database.

2.1.1 Microscopic problem

In the microscopic problem, a representative volume element (RVE) is considered, and the strain-stress data $(\bar{\boldsymbol{\varepsilon}}, \bar{\boldsymbol{\sigma}})$ is collected through computational homogenization on the RVE. Specially, the macroscopic strain $\bar{\boldsymbol{\varepsilon}}$ from each material data is applied to the RVE in the form of periodic boundary conditions [38], and the resulting microscopic stresses $\boldsymbol{\sigma}$ are averaged to obtain the equivalent macroscopic stress $\bar{\boldsymbol{\sigma}}$. The microscopic Cauchy stress $\boldsymbol{\sigma}$ and its conjugate strain $\boldsymbol{\varepsilon}$ are adopted, and the microscopic homogenization problem is formulated by

$$\int_{\omega} \boldsymbol{\sigma} : \delta \boldsymbol{\varepsilon} d\omega = 0 \quad (1a)$$

$$d\boldsymbol{\sigma} = \mathbb{C}_t^{(r)} : d\boldsymbol{\varepsilon} \quad (1b)$$

$$\mathbf{u}^+ - \mathbf{u}^- = \bar{\boldsymbol{\varepsilon}} \cdot (\mathbf{X}^+ - \mathbf{X}^-) \quad (1c)$$

$$\bar{\boldsymbol{\sigma}} = \frac{1}{|\omega|} \int_{\omega} \boldsymbol{\sigma} d\omega \quad (1d)$$

where ω is the domain of the RVE, $\mathbb{C}_t^{(r)}$ is the constitutive tensor of each material phase r . Eq. (1c) is the periodic boundary condition, which loads the macroscopic strain $\bar{\boldsymbol{\varepsilon}}$ to the boundary of RVE. The displacement is denoted by \mathbf{u} , the superscripts ‘+’ and ‘-’ specify two opposite surfaces of the RVE, and \mathbf{X} is the coordinate of the material point. Once $\bar{\boldsymbol{\varepsilon}}$ is given, Eqs. (1a) to (1c) can be solved using the Newton-Raphson method to get the deformed RVE. In post-processing, Eq. (1d) is used to compute the macroscopic Cauchy stress $\bar{\boldsymbol{\sigma}}$. In this manner, homogenized strain-stress data $(\bar{\boldsymbol{\varepsilon}}, \bar{\boldsymbol{\sigma}})$ can be generated and stored in the database $\bar{\mathcal{D}}$.

2.1.2 Macroscopic problem

For the macroscopic problem, a solid structure is considered. Its configuration is discretized with finite elements. At each integration point e , the data-driven solver seeks to minimize the distance between the corresponding strain-stress data $\bar{\mathbf{z}}_e^* = (\bar{\boldsymbol{\varepsilon}}_e^*, \bar{\boldsymbol{\sigma}}_e^*)$ in the material database $\bar{\mathcal{D}}$ and the admissible strain-stress state $\bar{\mathbf{z}}_e = (\bar{\boldsymbol{\varepsilon}}_e, \bar{\boldsymbol{\sigma}}_e)$ that satisfies equilibrium and compatibility. A distance-based functional formulates this constrained minimization problem by the cost function

$$\Pi = \frac{1}{2} \sum_{e=1}^m w_e \bar{\mathcal{F}}_e(\bar{\mathbf{z}}_e, \bar{\mathbf{z}}_e^*) - \bar{\boldsymbol{\eta}}^T \left(\sum_{e=1}^m w_e \bar{\mathbf{B}}_e \bar{\boldsymbol{\sigma}}_e - \bar{\mathbf{f}} \right) \quad (2)$$

where the distance is defined as

$$\bar{\mathcal{F}}_e(\bar{\mathbf{z}}_e, \bar{\mathbf{z}}_e^*) = (\bar{\boldsymbol{\varepsilon}}_e - \bar{\boldsymbol{\varepsilon}}_e^*)^T \bar{\mathbb{C}} (\bar{\boldsymbol{\varepsilon}}_e - \bar{\boldsymbol{\varepsilon}}_e^*) + (\bar{\boldsymbol{\sigma}}_e - \bar{\boldsymbol{\sigma}}_e^*)^T \bar{\mathbb{C}}^{-1} (\bar{\boldsymbol{\sigma}}_e - \bar{\boldsymbol{\sigma}}_e^*) \quad (3)$$

Here, $\bar{\boldsymbol{\eta}}$ is a vector of Lagrange multipliers enforcing the equilibrium constraints, $\bar{\mathbf{B}}_e$ is a matrix of interpolation functions prescribed by the finite element discretization, $\bar{\mathbf{f}}$ denotes the vector of nodal forces, w_e denotes the integration weight and m is the total number of integration points. Note that $\bar{\mathbb{C}}$ is a user-defined symmetric matrix to scale stress and strain to a similar magnitude, which does not represent a material behavior.

We take all possible variations of Eq. (2) considering the compatibility constraints $\bar{\boldsymbol{\varepsilon}}_e = \bar{\mathbf{B}}_e \bar{\mathbf{u}}$, resulting in the following linear equations

$$\sum_{e=1}^m w_e \bar{\mathbf{B}}_e^T \bar{\mathbb{C}} \bar{\mathbf{B}}_e \bar{\mathbf{u}} = \sum_{e=1}^m w_e \bar{\mathbf{B}}_e^T \bar{\mathbb{C}} \bar{\boldsymbol{\varepsilon}}_e^* \quad (4a)$$

$$\sum_{e=1}^m w_e \bar{\mathbf{B}}_e^T \bar{\mathbb{C}} \bar{\mathbf{B}}_e \bar{\boldsymbol{\eta}} = \bar{\mathbf{f}} - \sum_{e=1}^m w_e \bar{\mathbf{B}}_e^T \bar{\boldsymbol{\sigma}}_e^* \quad (4b)$$

The data-driven computing starts by randomly selecting data $\bar{\mathbf{z}}_e^*$ from the database $\bar{\mathcal{D}}$ for each integration point, followed by an iteration involving two steps. The first step is a mapping from $\bar{\mathbf{z}}_e^*$ to $\bar{\mathbf{z}}_e$ by solving the linear problem in Eq. (4). The second step is a reverse mapping from $\bar{\mathbf{z}}_e$ to $\bar{\mathbf{z}}_e^*$ via nearest-neighbor search, aiming at finding to find the closest material data $\bar{\mathbf{z}}_e^*$ in the database for each admissible data $\bar{\mathbf{z}}_e$

$$\bar{\mathcal{F}}_e(\bar{\mathbf{z}}_e, \bar{\mathbf{z}}_e^*) \leq \bar{\mathcal{F}}_e(\bar{\mathbf{z}}_e, \bar{\mathbf{z}}_e'), \quad \forall \bar{\mathbf{z}}_e' \in \bar{\mathcal{D}} \quad (5)$$

This requires distance calculations between $\bar{\mathbf{z}}_e$ and all the data $\bar{\mathbf{z}}_e' \in \bar{\mathcal{D}}$, then the optimal data $\bar{\mathbf{z}}_e^*$ is set to be the data $\bar{\mathbf{z}}_e'$ corresponding to the minimum distance. The overall iteration stops when the distance between $\bar{\mathbf{z}}_e$ to $\bar{\mathbf{z}}_e^*$ is minimized.

It should be emphasized that the nearest-neighbor search consumes a tremendous computational cost of distance calculation for a high-dimensional and high-density database. For a nearest-neighbor search involving a database with N data, each of dimension D , the complexity of the brute-force search on a classical computer is $O(ND)$. Related works show that efficient data structures can reduce the complexity [18, 34–36, 39] without significant loss of accuracy in data-driven computing. For instance, a k -d tree approach can substantially reduce the number of distance calculations, resulting in a complexity of approximately $O(\log(N)D)$ [34]. To further reduce the computational cost, the k -d tree will be used in this work, equipped with quantum computing for distance calculation introduced in the next section.

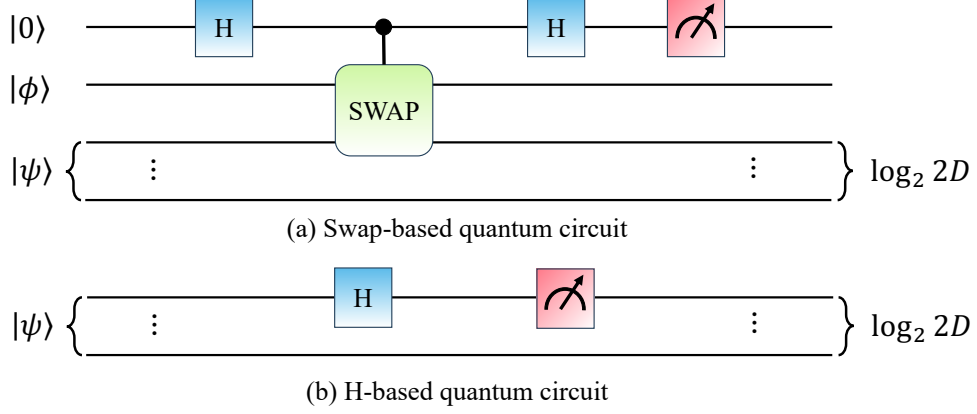


Figure 1: Quantum circuits of the two quantum algorithms.

2.2 Distance calculation via quantum computing

In this section, we present two quantum algorithms for distance calculation as well as their complexity analysis. The first one depends on the Swap test (Swap-based) and the second one depends on one Hadamard gate (H-based). Both of them can be used to calculate the Euclidean distance between two data and exponentially reduce the complexity. For simplicity, we denote the scaled admissible data $\bar{\mathbf{z}}_e$ as a vector \mathbf{V} and the scaled material data $\bar{\mathbf{z}}'_e$ as a vector \mathbf{V}' , and their dimensions are both D . Then, we can rewrite the distance in Eq. (3) as a squared Euclidean distance d

$$d = |\mathbf{V} - \mathbf{V}'|^2 \quad (6)$$

The two quantum algorithms for computing d are introduced in the following.

2.2.1 Quantum algorithms

Fig. 1 (a) presents the quantum circuit of the Swap-based algorithm for distance calculation. First, two quantum states containing the information of \mathbf{V} and \mathbf{V}' are encoded into the quantum computer via qRAM in time $O(\log D)$ [40, 41]

$$|\phi\rangle = \frac{1}{\sqrt{Z}}(|\mathbf{V}\rangle|0\rangle - |\mathbf{V}'\rangle|1\rangle) \quad (7a)$$

$$|\psi\rangle = \frac{1}{\sqrt{2}}(|0\rangle|\mathbf{V}\rangle + |1\rangle|\mathbf{V}'\rangle) \quad (7b)$$

where the Dirac notation $|\cdot\rangle$ denotes a quantum state, and $Z = |\mathbf{V}|^2 + |\mathbf{V}'|^2$. In addition, the amplitudes of the quantum states $|\mathbf{V}\rangle$ and $|\mathbf{V}'\rangle$ represent the normalized \mathbf{V} and \mathbf{V}' , respectively. Second, the swap test [42] is used to compute the inner product $|\langle\phi|\psi\rangle|^2$, which includes two Hadamard gates and one *CSWAP* gate. Note that the swap test consists of only three gates and has a time complexity of $O(1)$, independent of D . At the end of the circuit, the measurement result of the first qubit can be $|0\rangle$ or $|1\rangle$ due to the superposition of the quantum state, and the

probability of being $|0\rangle$ is

$$p_s = \frac{1}{2} + \frac{1}{2}|\langle\phi|\psi\rangle|^2 \quad (8)$$

By substituting Eq. (7) into Eq. (8), the distance is obtained by

$$d = 4Z(p_s - \frac{1}{2}) \quad (9)$$

To compute d using Eq. (9), we need to obtain Z and p_s , where Z is pre-computed in the classical computer [6] and p_s is calculated by running the swap test circuit. Due to the inherent properties of quantum systems, measuring a quantum state leads to its collapse [21], resulting in the acquisition of a single bit of classical information. This intrinsic property necessitates the execution of the quantum circuit multiple times and the use of statistical estimate to read out p_s [6]. Suppose we have n_m measurements, and the number of $|0\rangle$ in the measurement results is n_0 . According to the maximum-likelihood estimation, p_s is estimated by $\hat{p}_s = n_0/n_m$. By substituting \hat{p}_s in Eq. (9), we have

$$\hat{d} = 4Z(\frac{n_0}{n_m} - \frac{1}{2}) \quad (10)$$

where the estimated distance \hat{d} for d is obtained.

Fig. 1 (b) presents the quantum circuit of the H-based algorithm for distance calculation. Compared to the Swap-based algorithm, it requires fewer qubits and quantum gates, exhibiting noteworthy advantages. It only needs to prepare the quantum state $|\psi\rangle$ via qRAM in time $O(\log D)$

$$|\psi\rangle = \frac{1}{\sqrt{2}}(|0\rangle|\mathbf{V}\rangle + |1\rangle|\mathbf{V}'\rangle) \quad (11)$$

Then only one Hadamard gate is applied on the first qubit of $|\psi\rangle$, indicating a time complexity of $O(1)$. The probability of the measurement result of the first qubit being $|0\rangle$ is

$$p_h = \frac{1}{2} + \frac{1}{2}\langle\mathbf{V}|\mathbf{V}'\rangle \quad (12)$$

where the information of the inner product $\langle\mathbf{V}|\mathbf{V}'\rangle$ is contained in the probability. Then, by using the law of cosines, the distance is calculated by

$$d = Z - 2|\mathbf{V}||\mathbf{V}'|(2p_h - 1) \quad (13)$$

Similar to the Swap-based algorithm, multiple measurements of the first qubit are also needed to estimate p_h , i.e., if n_0 of the n_m measurements are $|0\rangle$, then p_h is estimated by $\hat{p}_h = n_0/n_m$. By substituting \hat{p}_h in Eq. (13), we have

$$\hat{d} = Z - 2|\mathbf{V}||\mathbf{V}'|\left(2\frac{n_0}{n_m} - 1\right) \quad (14)$$

where the estimated distance \hat{d} for d is obtained.

2.2.2 Complexity analysis

Given that both the Swap-based and H-based algorithms statistically estimate their respective probabilities, \hat{p}_s and \hat{p}_h , there inherently exists an estimation error that impacts the accuracy of the estimated distance \hat{d} . This section presents an analysis of the error and time complexity for these two quantum algorithms. Specifically, we derive the relationship between the root-mean-square error (RMSE) of the estimated distance \hat{d} and the number of measurements n_m used in each algorithm. It is crucial to note that this error analysis is focused solely on the statistical estimation aspects and does not account for potential inaccuracies arising from quantum hardware noise.

The derivations for the Swap-based and H-based algorithms are structurally similar. To simplify our presentation, we focus on the Swap-based algorithm in detail. The probability \hat{p}_s is estimated using maximum-likelihood estimation for the binomial distribution $n_0 \sim B(n_m, p_s)$, with $\hat{p}_s = n_0/n_m$. The expected value and variance of the random variable n_0 are given by $E(n_0) = n_m p_s$ and $\text{Var}(n_0) = n_m p_s (1 - p_s)$, respectively.

We then derive the mean of the estimated distance \hat{d} from Eq. (10) as follows

$$E(\hat{d}) = 4Z \left(\frac{n_m p_s}{n_m} - \frac{1}{2} \right) = d \quad (15)$$

This indicates that the estimation of \hat{d} is unbiased. Correspondingly, the squared RMSE of \hat{d} , denoted by ϵ_s^2 , equates to the variance of \hat{d} from Eq. (10)

$$\epsilon_s^2 = 16 (|\mathbf{V}|^2 + |\mathbf{V}'|^2)^2 \frac{p_s(1 - p_s)}{n_m} \quad (16)$$

Similarly, for the H-based algorithm, we derive the squared RMSE of the estimated distance \hat{d} from Eq. (14), denoted by ϵ_h^2

$$\epsilon_h^2 = 16 |\mathbf{V}|^2 |\mathbf{V}'|^2 \frac{p_h(1 - p_h)}{n_m} \quad (17)$$

Therefore, we have $\epsilon_s^2 \sim O(1/n_m)$ and $\epsilon_h^2 \sim O(1/n_m)$. Equivalently, the upper bounds of n_m for the two algorithms scale the same, i.e., $n_m \sim O(1/\epsilon_s^2)$ for the Swap-based algorithm and $n_m \sim O(1/\epsilon_h^2)$ for the H-based algorithm. Given that the time complexities for executing the circuits once for both algorithms are $O(\log D)$, the upper bounds of the total time for these quantum algorithms are also equivalent, namely $O(\log D/\epsilon_s^2)$ for the Swap-based algorithm and $O(\log D/\epsilon_h^2)$ for the H-based algorithm. Hence, both quantum algorithms can exponentially reduce the computational complexity of distance calculation from $O(D)$ to $O(\log D)$.

Though the upper bounds of ϵ_s^2 and ϵ_h^2 scale the same, we have an interesting finding that there exists a relation $\epsilon_h^2 \leq \epsilon_s^2$, i.e., the H-based algorithm has a lower estimation error than the Swap-based algorithm under the same n_m and regardless of the quantum hardware noise. Here we present the proof of this relation. From Eqs. (16) and (17), the relation $\epsilon_h^2 \leq \epsilon_s^2$ is

equivalent to

$$16|\mathbf{V}|^2|\mathbf{V}'|^2\frac{p_h(1-p_h)}{n_m} \leq 16(|\mathbf{V}|^2 + |\mathbf{V}'|^2)^2\frac{p_s(1-p_s)}{n_m} \quad (18)$$

By eliminating n_m and replacing p_h and p_s using the relations in Eqs. (9) and (13), we have

$$4|\mathbf{V}|^2|\mathbf{V}'|^2 - Z^2 + 2dZ - d^2 \leq 4Z^2 - d^2 \quad (19)$$

which can be further simplified as

$$4|\mathbf{V}|^2|\mathbf{V}'|^2 - 4\cos(\theta)|\mathbf{V}||\mathbf{V}'|(|\mathbf{V}|^2 + |\mathbf{V}'|^2) - 3(|\mathbf{V}|^2 + |\mathbf{V}'|^2)^2 \leq 0 \quad (20)$$

where $\cos(\theta)$ is the cosine of the angle between \mathbf{V} and \mathbf{V}' , and $\cos(\theta) \in [-1, 1]$. Thus, the sufficient condition of Eq. (20) is

$$4|\mathbf{V}|^2|\mathbf{V}'|^2 + 4|\mathbf{V}||\mathbf{V}'|(|\mathbf{V}|^2 + |\mathbf{V}'|^2) - 3(|\mathbf{V}|^2 + |\mathbf{V}'|^2)^2 \leq 0 \quad (21)$$

Without loss of generality, we set $|\mathbf{V}'| = k|\mathbf{V}|$, where $k \geq 0$. Then Eq. (21) can be simplified as

$$-3k^4 + 4k^3 - 2k^2 + 4k - 3 \leq 0 \quad (22)$$

which can be easily proved since the left-hand side only has one critical point at $k = 1$ and the corresponding value is 0. Therefore, we have proved that $\epsilon_h^2 \leq \epsilon_s^2$. We would like to mention that this proof only demonstrates that the H-based algorithm has a lower estimation error without the consideration of quantum hardware noise. When the quantum hardware noise is considered, this advantage may not be obvious, as illustrated in Section 3.1.

In conclusion, both quantum algorithms can reduce the computational complexity of distance calculation from $O(D)$ to $O(\log D)$. By using these quantum algorithms, the complexity of the nearest-neighbor search in data-driven computing is reduced to $O(D + N \log(D))$ [6]. In addition, the simulations in this work are conducted with the k -d tree structure presented in Appendix A to reduce the number of queries at the same time, resulting in a more favorable complexity $O(D + \log(N) \log(D))$. In the next section, the zero-noise extrapolation technique (referred to as ZNE) is employed to mitigate the error caused by quantum hardware noise, thereby improving the accuracy of the quantum algorithms in distance calculation. For clarity in subsequent sections, the probabilities derived from Swap-based and H-based algorithms will no longer be distinguished. Instead, the true and estimated probabilities are denoted as p and \hat{p} , respectively.

2.3 Zero-noise extrapolation

While quantum computing has demonstrated a remarkable exponential reduction in computational complexity, the accuracy of current devices of quantum computing is influenced by hardware noise [28], leading to challenges in extracting precise and effective information. Specifically, the estimated \hat{p} will be biased from the true p , causing an error in the calculated distance.

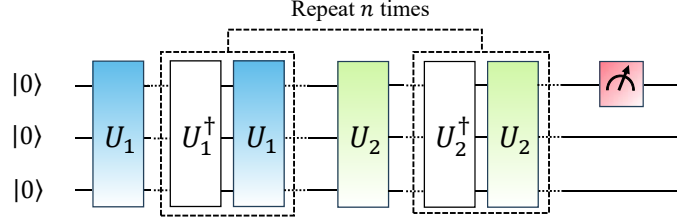


Figure 2: Sketch of the folding circuit.

Here, the zero-noise extrapolation is applied to improve the accuracy of the distance calculation. It offers a way to mitigate quantum hardware noise without the need for additional qubit resources and detailed knowledge of quantum processors. The main idea of ZNE is to intentionally scale up the hardware noise so as to obtain the estimated \hat{p} with different noise levels. Then the obtained results are processed on a classical computer to extrapolate the noiseless value. In the following, we will introduce the details of ZNE, which can be implemented in two steps: noise-scaling and extrapolation [43].

2.3.1 Scaling up the noise

The first step aims to scale up the hardware noise while still allowing the quantum circuit to perform distance calculation. To achieve this, the quantum circuit of the Swap-based or the H-based algorithm requires to be modified by folding each quantum gate in it. Here, we use U to represent an arbitrary quantum gate in the circuit, e.g., the Hadamard gate in the circuit of the Swap-based algorithm. Then the folding of the gate is represented by

$$U \longrightarrow U(U^\dagger U)^i \quad (23)$$

where U^\dagger is the conjugate transpose of U and i is a positive integer representing the number of foldings. If all the gates are noiseless, the gate folding has no effect on the final output since $U^\dagger U$ is equal to the identity operator [21]. However, on a quantum computer with hardware noise, the gate folding will lead to an increasing noise with a factor $\lambda = 1 + 2i$, which corresponds to the total number of gates in the folding circuit. Hence, we can construct a folding circuit by repeating each gate of the quantum algorithm (see Fig. 2), and perform measurements on the quantum circuit to get the estimated probability \hat{p} with higher noise. By controlling the number of foldings i from 0 to a maximum folding number n to build a set of quantum circuits, we can get the estimated $\hat{\mathbf{p}} = \{\hat{p}_0, \hat{p}_1, \dots, \hat{p}_n\}$ corresponding to a set of noise scale factors $\lambda = \{1, 3, \dots, 1 + 2n\}$.

In the following, we will illustrate the influence of gate folding on the estimated \hat{p} with noisy quantum computing, which requires deriving the relation between \hat{p} and λ . We would like to mention that, for all the numerical examples in this work, the quantum hardware noise model including depolarizing channel and thermal relaxation is employed, and their parameters are obtained from IBM's real device (see Appendix B). Here, for simplicity in demonstration, only the single-qubit depolarizing channel is employed in the following derivations. The density

matrix is used to describe the mixed quantum state concerning decoherence. Firstly, we consider a single qubit density matrix ρ , whose evolution with an noiseless gate U is expressed as

Noiseless gate:

$$\rho \xrightarrow{U} U\rho U^\dagger \quad (24)$$

Then we consider the hardware noise of depolarizing channel. If we define that the probability of the qubit being depolarized is q , then a noisy gate U applying to the density matrix can be described as

Noisy gate ($\lambda = 1$):

$$\rho \xrightarrow{U} (1 - \frac{3}{4}q)U\rho U^\dagger + \frac{q}{4} \sum_{j=1}^3 (UG_j)\rho(UG_j)^\dagger, \quad G = \{X, Y, Z\} \quad (25)$$

where $G = \{X, Y, Z\}$ are three Pauli gates, respectively to a rotation around the x , y and z axes of the Bloch sphere by π radians [21]. For simplicity, the second term of Eq. (25) is set to $\rho^*(q) = \frac{q}{4} \sum_{j=1}^3 (UG_j)\rho(UG_j)^\dagger$, which represents a mixed state. Then Eq. (25) can be rewritten as

Noisy gate ($\lambda = 1$):

$$\rho \xrightarrow{U} (1 - \frac{3}{4}q)U\rho U^\dagger + \rho^*(q) \quad (26)$$

Now we consider folding the gate once, which means we need to apply two additional gates U^\dagger and U . First, we apply the noisy gate U^\dagger

Noisy gate ($\lambda = 2$):

$$\begin{aligned} \rho &\xrightarrow{UU^\dagger} (1 - \frac{3}{4}q)U^\dagger((1 - \frac{3}{4}q)U\rho U^\dagger + \rho^*(q))U + \\ &\quad \frac{q}{4} \sum_{j=1}^3 (UG_j)^\dagger((1 - \frac{3}{4}q)U\rho U^\dagger + \rho^*(q))(UG_j) \\ &= (1 - \frac{3}{4}q)^2\rho + (1 - \frac{3}{4}q)U^\dagger\rho^*(q)U + \\ &\quad \frac{q}{4} \sum_{j=1}^3 (UG_j)^\dagger((1 - \frac{3}{4}q)U\rho U^\dagger + \rho^*(q))(UG_j) \\ &= (1 - \frac{3}{4}q)^2\rho + \rho^*(q, q^2) \end{aligned} \quad (27)$$

where $\rho^*(q, q^2)$ is a density matrix related to the linear combination of q and q^2 . Then we

consider another noisy gate U to finish the folding

Noisy gate ($\lambda = 3$):

$$\begin{aligned}
\rho &\xrightarrow{UU^\dagger U} (1 - \frac{3}{4}q)U((1 - \frac{3}{4}q)^2\rho + \rho^*(q, q^2))U^\dagger + \\
&\quad \frac{q}{4}\sum_{j=1}^3(UG_j)((1 - \frac{3}{4}q)^2\rho + \rho^*(q, q^2))(UG_j)^\dagger \\
&= (1 - \frac{3}{4}q)^3U\rho U^\dagger + (1 - \frac{3}{4}q)U\rho^*(q, q^2)U^\dagger + \\
&\quad \frac{q}{4}\sum_{j=1}^3(UG_j)((1 - \frac{3}{4}q)^2\rho + \rho^*(q, q^2))(UG_j)^\dagger \\
&= (1 - \frac{3}{4}q)^3U\rho U^\dagger + \rho^*(q, q^2, q^3)
\end{aligned} \tag{28}$$

One can see that after folding once, ρ^* is related to a higher order of q^3 . Furthermore, if we consider folding n times, the derivation of the folding can be generalized as

Noisy gate ($\lambda = 1 + 2n$):

$$\rho \xrightarrow{U(U^\dagger U)^n} (1 - \frac{3}{4}q)^\lambda U\rho U^\dagger + \rho^*(q, q^2, \dots, q^\lambda) \tag{29}$$

Eq. (29) corresponds to the folding of a single-qubit gate. Moreover, we generalize the gate folding for an arbitrary circuit, which is assumed to contain m_s single-qubit gates and m_t two-qubit gates. In total, there will be $m_d = m_s + 2m_t$ times of single depolarizing acting on the qubits

Noisy circuit ($\lambda = 1 + 2n$):

$$\rho \xrightarrow{\text{circuit}} (1 - \frac{3}{4}q)^{m_d\lambda} U\rho U^\dagger + \rho^*(q^1, q^2, \dots, q^{m_d\lambda}) \tag{30}$$

where the density matrix ρ is considered as the outer product of the initial quantum state $|0\phi\psi\rangle\langle 0\phi\psi|$. To obtain the probability of the first qubit measured to be $|0\rangle$, we need to sum the related diagonal elements of the final density matrix [21] in Eq. (30)

$$\hat{p}(\lambda) = (1 - \frac{3}{4}q)^{m_d\lambda} p + \sum_{j=1}^{m_d\lambda} p_j^* q^j \tag{31}$$

where \hat{p} is the probability concerning hardware noise, p is the true probability computed from the density matrix $U\rho U^\dagger$, and p_j^* are values computed from $\rho^*(q^1, q^2, \dots, q^{m_d\lambda})$. One notes that the coefficient of the first term $(1 - \frac{3}{4}q)^{m_d\lambda}$ will approach zero with the increasing noise scale factor λ , which means the information of p gradually loses. In addition, this theoretical derivation is different from that in the work of Giurgica-Tiron et al. [43]. The reason is that their derivation is under the assumption of global depolarizing noise affecting all qubits, while this derivation considers depolarizing noise for each single qubit.

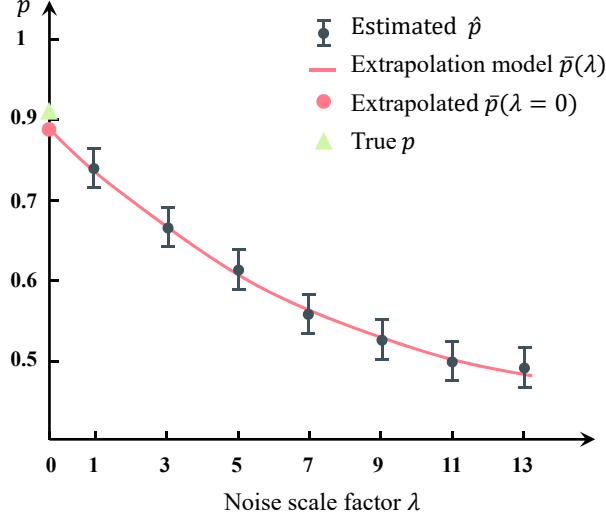


Figure 3: Sketch of the extrapolation method.

2.3.2 Extrapolating the noiseless probability

The second step of ZNE intends to extrapolate the noiseless probability based on the estimated $\hat{\mathbf{p}} = \{\hat{p}_0, \hat{p}_1, \dots, \hat{p}_n\}$ under different noise scale factors $\boldsymbol{\lambda} = \{1, 3, \dots, 1 + 2n\}$, which is processed on a classical computer. As shown in Fig. 3, this extrapolation requires a model $\bar{p}(\lambda)$ to characterize the relationship between \hat{p} and λ . After fitting this model with $\hat{\mathbf{p}}$ and $\boldsymbol{\lambda}$, the noiseless value is predicted as $\bar{p}(\lambda = 0)$. One straightforward thought is to directly derive the relation between \hat{p} and λ considering various noise models shown in Appendix B, and then the derived relation is employed as the extrapolation model $\bar{p}(\lambda)$. However, even for the relation in Eq. (31) that only considers the single-qubit depolarizing channel, it is already hard to fit since the number of terms in $\sum_{j=1}^{m_d \lambda} p_j^* q^j$ changes depending on the value of λ , let alone more noise models are considered. Another approach is to assume a relatively concise model between the estimated \hat{p} and the noise scale factor λ , which is the core concept of ZNE. Here, we present four extrapolation models, i.e., linear extrapolation, quadratic extrapolation, exponential extrapolation and Richardson extrapolation, which are commonly used in ZNE [43]

$$\begin{aligned}
\text{Linear extrapolation :} \quad & \bar{p}^{\text{linear}}(\lambda) = c_0 + c_1 \lambda \\
\text{Quadratic extrapolation :} \quad & \bar{p}^{\text{quad}}(\lambda) = c_0 + c_1 \lambda + c_2 \lambda^2 \\
\text{Exponential extrapolation :} \quad & \bar{p}^{\text{exp}}(\lambda) = c_0 + c_1 e^{-c_2 \lambda} \\
\text{Richardson extrapolation :} \quad & \bar{p}^{\text{Rich}}(\lambda) = c_0 + c_1 \lambda + \dots + c_n \lambda^n
\end{aligned} \tag{32}$$

where c_0, c_1, \dots, c_n are the fitting coefficients. The linear, quadratic and Richardson extrapolations all belong to polynomial models. The difference lies in that the highest order of linear and quadratic extrapolations are fixed, while the highest order of the Richardson n is related to the number of elements in the estimated probabilities $\hat{\mathbf{p}} = \{\hat{p}_0, \hat{p}_1, \dots, \hat{p}_n\}$. For example, the Richardson extrapolation will degenerate into the linear one when $n = 1$, and will degenerate into the quadratic one when $n = 2$. The coefficients of these models are determined via the

least squares fitting, i.e., finds optimal coefficients that minimize the sum of squared residuals $\sum_{i=0}^n (\hat{p}_i - \bar{p}(\lambda = 1 + 2i))^2$. Then the noiseless value can be predicted by $\bar{p}(\lambda = 0)$. Finally, we substitute $\bar{p}(\lambda = 0)$ into the distance expression of the Swap-based algorithm Eq. (10) or the H-based algorithm Eq. (14), resulting in the mitigated distance \bar{d} .

The performance of these extrapolation models will be validated in Section 3.1. We would like to mention that ZNE is used to handle the hardware noise associated with quantum gates, instead of the estimation error arising from the statical estimation of \hat{p} , which is presented by the grey intervals in Fig. 3. However, the estimation error may affect the performance of ZNE, since a larger value of n_m leads to lower estimation error, resulting in a higher accuracy of the estimated \hat{p} . The influence of n_m on error mitigation will be discussed later in Section 3.1. In addition, the flowchart of the distance calculation via error-mitigated quantum computing is detailed in Algorithm 1.

Algorithm 1 Distance calculation via error-mitigated quantum computing

Require: Vectors \mathbf{V} , \mathbf{V}' ; $|\mathbf{V}|^2$; $|\mathbf{V}'|^2$; Number of measurements n_m ;

Maximum folding number n

Step 1: Noise-scaling

for $i = 0$ to n **do**

 Fold each quantum gate of the Swap-based circuit or the H-based circuit i times

 Save the noise scale factor $\lambda = 1 + 2i$ to the set $\boldsymbol{\lambda}$

for $t = 1$ to n_s **do**

 Run the circuit and measure the first qubit on a quantum computer

end for

 Set n_0 as the number of 0s in the measurement results

 Estimate the probability $\hat{p} = n_0/n_s$ and save it to the set $\hat{\mathbf{p}}$

end for

Step 2: Extrapolation

Choose an extrapolation model $\bar{p}(\lambda)$

Fit $\bar{p}(\lambda)$ with $\hat{\mathbf{p}}$ and $\boldsymbol{\lambda}$

Extrapolate the noiseless value $\bar{p}(\lambda = 0)$

Compute the mitigated distance \bar{d} using Eq. (10) or Eq. (14)

3 Validation

In this section, numerical tests are carried out to validate the proposed data-driven method with error-mitigated quantum computing (referred to as mitigated qDD). First, we evaluate the performance of the Swap-based and the H-based algorithms in distance calculation considering hardware noise. Second, ZNE is employed in the two quantum algorithms and the performance of different extrapolation models on error mitigation are compared. Finally, a roof truss structure is used to validate the effectiveness of the mitigated qDD. Since the availability of real quantum computers is currently limited, the numerical tests in this paper are all carried out based on the quantum computer simulator Qiskit developed by IBM [37]. To reflect the actual operation of

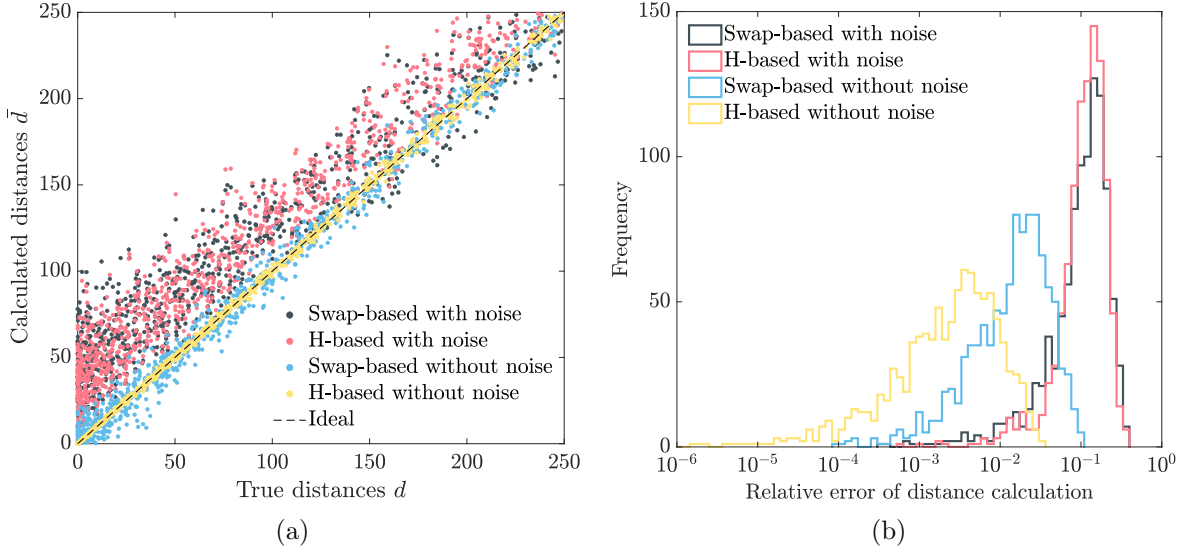


Figure 4: Results of the calculated distances with and without quantum hardware noise. (a) True distances versus calculated distances. (b) Frequency of the relative errors.

a quantum computer, the quantum gates in circuits are transpiled into a standard set of basic gates $\{I, X, SX, RZ, ECR\}$, which are compatible with real quantum devices. Considering that qRAM is not yet available [44, 45], a series of quantum gates are used to prepare the quantum states [46] in the two algorithms for distance calculation, and hardware noise is also considered in these gates and mitigated by ZNE. The folding circuit in ZNE is constructed based on the transpiled circuit. To simulate the hardware noise, each gate in the circuit is associated with a depolarizing noise followed by a thermal relaxation noise, and the noise parameters are obtained from the IBM’s real device *ibm_osaka*, as shown in Appendix B. In addition, we use the normal approximation to accelerate the statistical estimation of \hat{p} on the quantum computer simulator, as shown in Appendix C.

3.1 Evaluation of the two quantum algorithms

The performance of the Swap-based and the H-based quantum algorithms in distance calculation is first evaluated, where the results with and without hardware noise are both presented. We randomly sample 1000 vector pairs $(\mathbf{V}, \mathbf{V}')$ in a 6-dimensional space, such that their distances $d = \|\mathbf{V} - \mathbf{V}'\|^2$ obey the uniform distribution. The Swap-based algorithm requires 6 qubits and has a circuit depth of around 100, whereas the H-based algorithm necessitates 4 qubits with a circuit depth of around 70. For both algorithms, the number of measurements n_m is set to 10^4 .

Fig. 4 (a) represents the true distances versus calculated distances from the 1000 vector pairs. As a reference, the dashed line marked with ‘Ideal’ is drawn according to the relation $\bar{d} = d$, meaning results closer to the dashed line exhibit higher accuracy. Fig. 4 (b) shows the distribution of relative errors $|\bar{d} - d|/d_{\max}$, where d_{\max} refers to the maximum value of d . In summary, the results considering hardware noise exhibit a larger error for both algorithms,

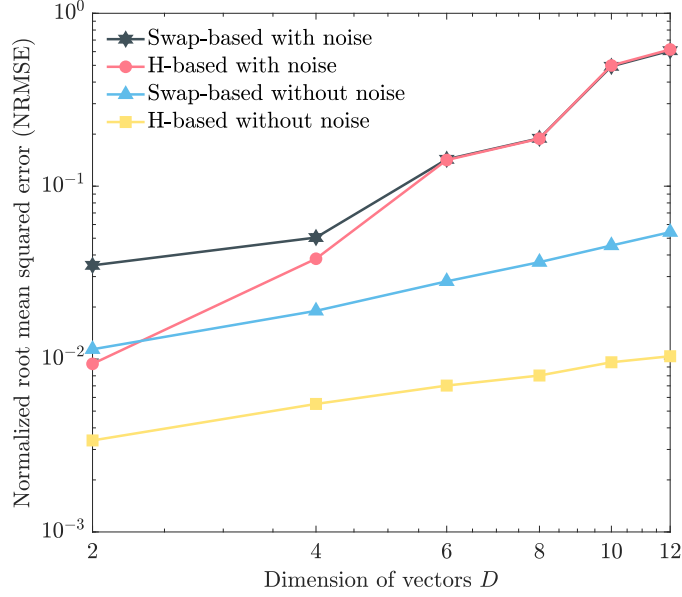


Figure 5: Dimension of vectors D versus the normalized root mean squared error (NRMSE) of the calculated distances.

compared to the results without noise. Specifically, the relative errors for both algorithms increase from around 10^{-2} to around 10^{-1} due to hardware noise. If the hardware noise is not considered, the H-based algorithm exhibits smaller errors than the Swap-based one, which is consistent with the error analysis in Section 2.2.2. However, when hardware noise is taken into account, the error distributions of the two algorithms are almost the same. This appears counterintuitive, as the Swap-based algorithm should have a lower accuracy since it employs more quantum gates with hardware noise. We believe the reason is that both algorithms require $O(D)$ layers of quantum gates to prepare the quantum state $|\psi\rangle$ [46]. As the dimension D increases, the depth of the circuit for state preparation increases linearly, while the depth of the rest of the circuit remains unchanged. Therefore, state preparation gradually takes a significant portion of the entire circuits for both algorithms. In this case, the hardware noise introduced during the state preparation becomes the predominant source of error in distance calculations, resulting in a similar accuracy for the two algorithms.

To confirm the above explanation, the relationship between the dimension of vectors D and the accuracy of distance calculations is presented in Fig. 5. The normalized root mean squared error (NRMSE), defined as $\sqrt{\sum(\bar{d} - d)^2 / (1000d_{\max}^2)}$, is used to reflect the average accuracy. As D increases from 2 to 12, the portion of the state preparation in the entire circuit increase from 11/43 (26%) to 212/244 (87%) for the Swap-based algorithm, and from 10/13 (77%) to 212/215 (99%) for the H-based algorithm. This shows that as D increases, the state preparation takes the majority of the proportion of the whole circuit. Correspondingly, if hardware noise is taken into account, the accuracy of the two quantum algorithms tends to be the same as shown in Fig. 5, which provides evidence for the above explanation.

In conclusion, the above analysis shows that hardware noise reduces the accuracy of distance calculations in both the Swap-based and H-based quantum algorithms. In the subsequent

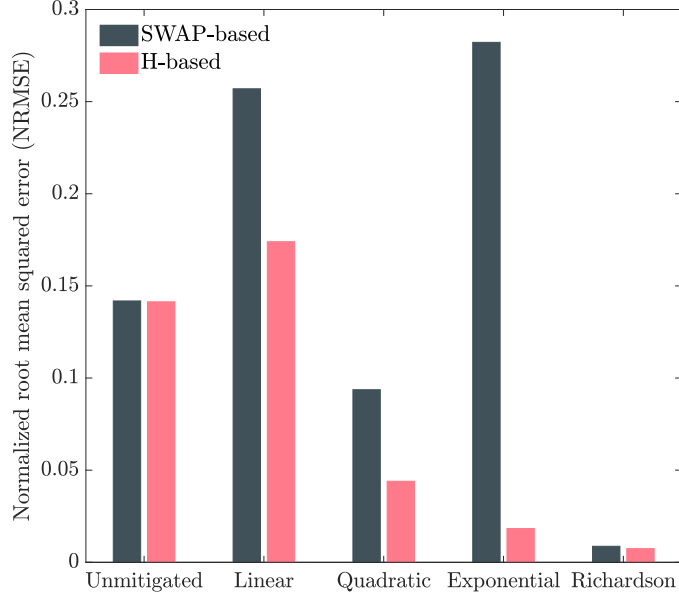


Figure 6: Normalized root mean squared error (NRMSE) of the calculated distances with ZNE.

section, we explore the application of the ZNE, aiming to improve the accuracy of distance calculations.

3.2 Performance of ZNE

In this section, the performance of ZNE in error mitigation for the two quantum algorithms is investigated. We use the linear, quadratic, exponential, and Richardson extrapolation models to predict noiseless probability $\bar{p}(\lambda = 0)$ and then calculate the mitigated distance \bar{d} . First, the number of measurements n_m is set to 10^8 and the maximum folding number n is set to 6, which means $\lambda = \{1, 3, \dots, 13\}$ and $\hat{p} = \{\hat{p}_0, \hat{p}_1, \dots, \hat{p}_6\}$ are used to fit each extrapolation model $\bar{p}(\lambda)$. As shown in Fig. 6, the Richardson extrapolation model demonstrates superior performance across all models. It can reduce the NRMSE from 14.18% to 0.87% for the Swap-based algorithm, and from 14.14% to 0.74% for the H-based algorithm, resulting in a similar level of accuracy for the two algorithms. This validates the effectiveness of ZNE in improving the accuracy of distance calculation. We believe that the Richardson extrapolation model outperforms the other three models primarily due to its inclusion of more fitting coefficients, which enhance its fitting capabilities.

Moreover, we investigate the effect of n_m on the performance of ZNE, where a larger value of n_m leads to a lower estimation error of \hat{p} , as mentioned in Section 2.2.2. Fig. 7 (a) and Fig. 7 (b) respectively present the influence of n_m on the NRMSE of the Swap-based and the H-based algorithm, where the maximum folding number n is set to 6. For both the Swap-based and the H-based algorithms, the performance of linear, quadratic, and exponential extrapolations are almost unaffected by n_m , while the performance of Richardson extrapolation shows a strong correlation with respect to n_m , i.e., its accuracy is improved with an increasing n_m and tends to be converged when n_m is about 10^{10} . The reason is that Richardson extrapolation has more

fitting coefficients than the other three models. On one hand, it leads to a higher ability to represent a complex relationship between \hat{p} and λ . On the other hand, it is more sensitive to the estimation error. This is consistent with the results in [28], where it is found that the Richardson extrapolation is sensitive to the variance of the unmitigated measurements. Therefore, the Richardson extrapolation can accurately predict the noiseless $\bar{p}(\lambda = 0)$ and the mitigated \bar{d} with a large n_m , and shows large errors with a small n_m .

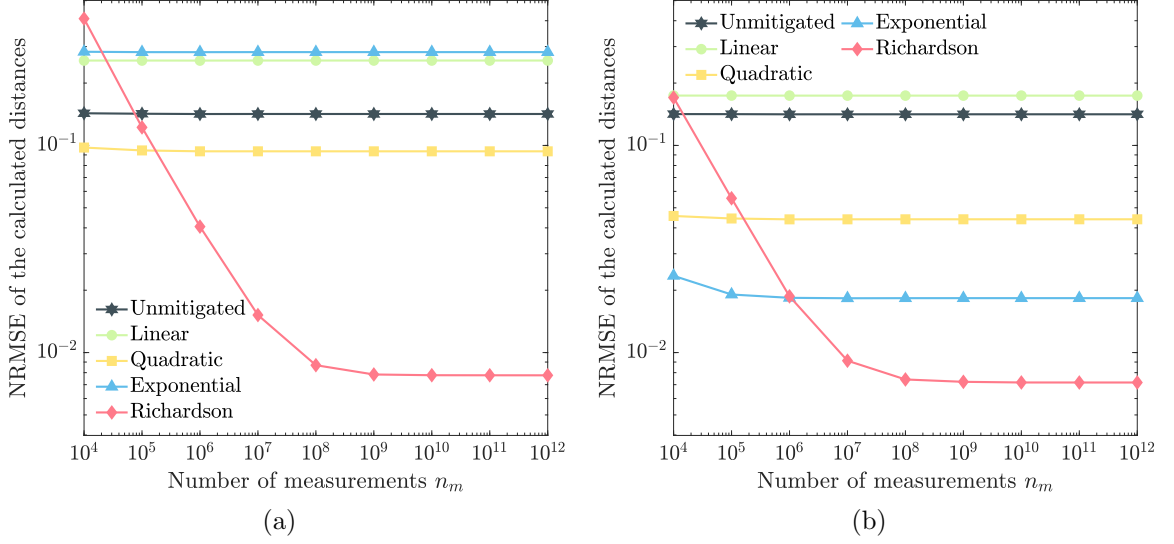


Figure 7: Influence of the number of measurements n_m on the (a) Swap-based and (b) H-based algorithms with ZNE.

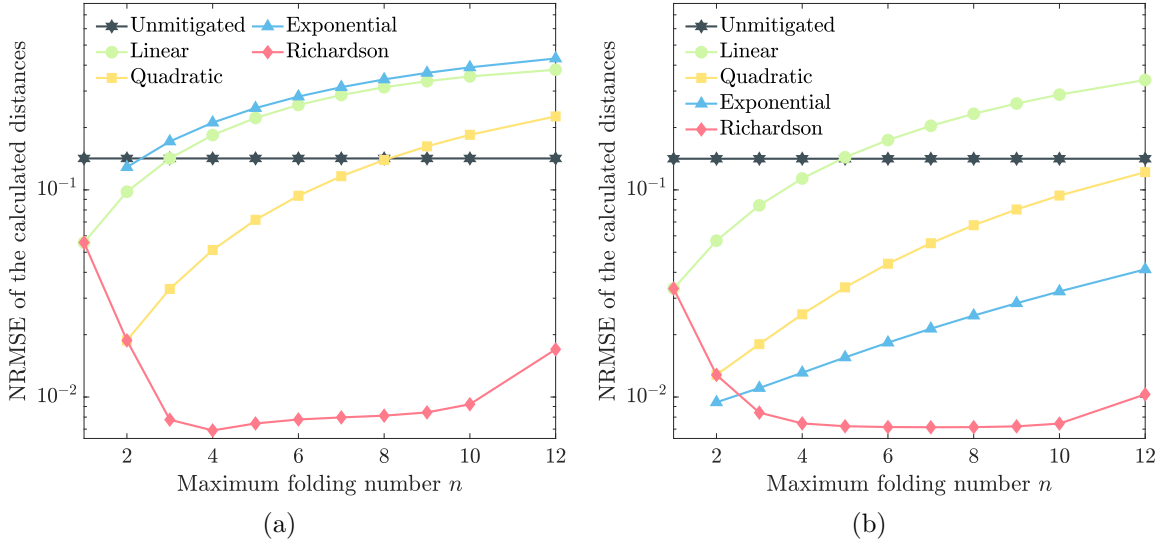


Figure 8: Influence of maximum folding number n on the (a) Swap-based and (b) H-based algorithms with ZNE.

Furthermore, we investigate the influence of the maximum folding number n on the performance of ZNE, where the number of measurements n_m is set to 10^{10} . As shown in Fig. 8 (a)

and Fig. 8 (b), the performance of ZNE is sensitive to the maximum folding number n . The accuracy of the distance calculations with linear, quadratic, and exponential extrapolations decreases with the increasing n . Whereas the accuracy of the distance calculations with Richardson extrapolations reaches an optimum at $n = 4$ for the Swap-based algorithm and $n \in [5, 9]$ for the H-based algorithm. We would like to mention that the approaches for optimizing n deserve future investigations [47].

In conclusion, the numerical results demonstrate the effectiveness of ZNE in improving the accuracy of distance calculation with noisy quantum computing. Although the two algorithms can reach a similar level of accuracy with the help of ZNE, the H-based algorithm consumes fewer qubits and quantum gates compared to the Swap-based algorithm, exhibiting an advantage for the NISQ quantum computers. Hence, ZNE with the H-based algorithm is utilized in subsequent numerical simulations, and the corresponding n and n_m are set to 5 and 10^{10} , respectively.

Remark. Compared to the H-based algorithm, the Swap-based algorithm has a unique ability to reduce the complexity of distance calculation between one data and the center of a cluster of data [31]. However, the application of this ability is limited by the requirement of data normalization. One potential application is to construct the efficient k -means data structure for the material database [18], where the complexity of a standard k -means algorithm on a classical computer is $O(kND)$ for one iteration. However, to use the Swap-based algorithm, all the data are required to be normalized in the first place, which already takes $O(ND)$, eliminating the complexity advantage of quantum computing. Regarding another potential application in data search concerning k -means data structure [18], the standard way is to directly calculate the distance between the admissible point and the center of a cluster of data, where the latter is already computed offline in advance. Therefore, there is no obvious advantage to using the Swap-based algorithm in this case either. When the center of a cluster of data can not be computed offline in advance, such as in the case of on-the-fly material data sampling [17], the application of the Swap-based algorithm is once again prevented by the need for data normalization, since the data is newly generated. In future research, investigating an efficient quantum algorithm for distance calculation that does not require data normalization could be valuable. In addition, we believe the unique advantage of the Swap-based algorithm in data-driven computing deserves future exploration.

3.3 Roof truss

In this section, a roof truss is considered to validate the performance of ZNE in data-driven simulation with noisy quantum computing. Here, the H-based algorithm is employed for distance calculation, and it necessitates 2 qubits with a circuit depth of around 15 without folding. The configuration of the roof truss is shown in Fig. 9. All the bars have the same cross-sectional area $A = 100 \text{ mm}^2$. The displacement of node 1 is fixed in the x and y directions, while the node 7 is fixed in the y direction. The nodes 2, 4 and 6 are under the loads $P = 200 \text{ N}$.

The material of the roof is assumed to satisfy a Ramberg-Osgood material model, and the material database is collected by uniformly sampling the stress data in the range $\sigma \in [-6, 6] \text{ MPa}$

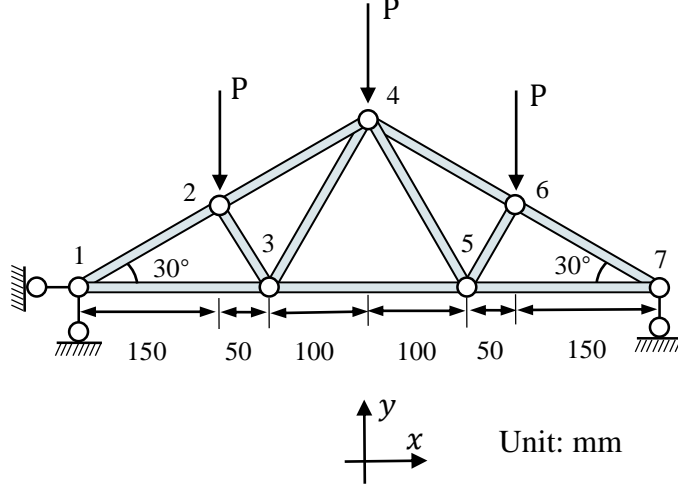


Figure 9: Sketch of the roof truss.

and obtaining the corresponding strain data ϵ via the following relation

$$\epsilon = \frac{\sigma}{E} + \alpha \frac{\sigma}{E} \left(\frac{|\sigma|}{\sigma_0} \right)^{\beta-1} \quad (33)$$

where $E = 10000$ MPa refers to Young's modulus, $\alpha = 0.5$ the yield offset, $\sigma_0 = 5$ MPa the yield stress and $\beta = 3$ the hardening exponent. In this way, a material database with 161 data is generated. Furthermore, a k -d tree data structure is used to reduce the number of distance calculations in data-driven computing. The analytical solution is used as the reference result, and a root-mean-square (RMS) error of stress σ_{RMS} is employed to evaluate the accuracy of solutions

$$\sigma_{\text{RMS}} = \sqrt{\frac{\sum_{e=1}^m w_e (\sigma_e - \sigma_e^{\text{ref}})^2}{\sum_{e=1}^m w_e (\sigma_e^{\text{ref}})^2}} \quad (34)$$

Firstly, the performance of the data-driven methods based on classical computing (classical DD), noisy quantum computing (unmitigated qDD), and error-mitigated quantum computing (mitigated qDD) are evaluated. Fig. 10 presents the evolution of the global distance $\bar{\mathcal{F}} = \frac{1}{2} \sum_{e=1}^m w_e \bar{\mathcal{F}}_e(\bar{\mathbf{z}}_e, \bar{\mathbf{z}}_e^*)$ during the data-driven computing process, which is defined as the sum of the distances at all the integral points [7]. The mitigated qDD can accurately predict the stress of each bar ($\sigma_{\text{RMS}} = 0.76\%$), which is comparable to that of a classical DD ($\sigma_{\text{RMS}} = 0.92\%$). In comparison, although the unmitigated qDD also converged, the obtained result shows noticeable discrepancies from the reference solution ($\sigma_{\text{RMS}} = 4.55\%$). This means that ZNE can effectively improve the accuracy of qDD with noisy quantum computing.

Furthermore, the effectiveness of the k -d tree data structure in accelerating qDD is verified. Fig. 11 shows the RMS error of the stress and the average number of distance calculations

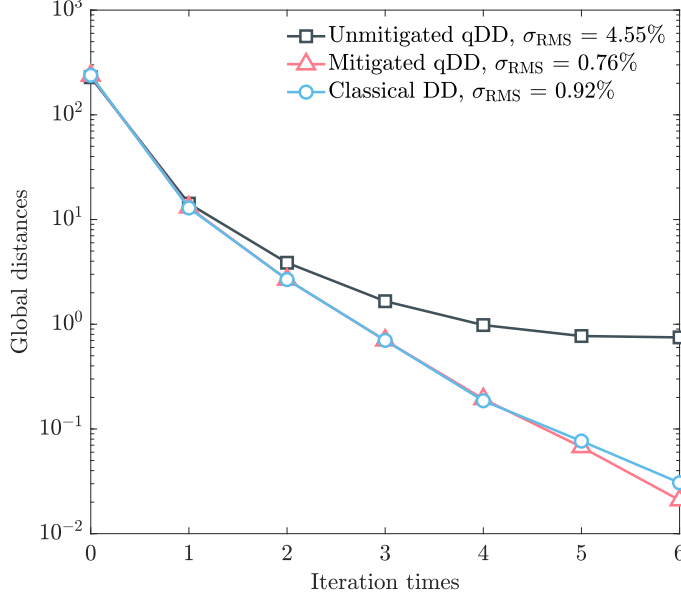


Figure 10: Global distances obtained by unmitigated qDD, mitigated qDD and classical DD.

Table 1: Root-mean-square (RMS) error of the stress versus the number of measurements n_m for the mitigated and unmitigated qDD.

Classical DD	0.92%		
	$n_s = 10^6$	$n_s = 10^8$	$n_s = 10^{10}$
Mitigated qDD	4.79%	1.56%	0.76%
Unmitigated qDD	5.10%	4.36%	4.55%

per nearest-neighbor search versus the number of data in the database. Compared to the full database without data structure, the k -d tree database can achieve the same level of accuracy while significantly reducing the number of distance calculations. We would like to emphasize that the results show opportunities for combining a variety of efficient data structures [18, 35, 36, 48] with qDD, resulting in accelerations in both the number of data N and the dimension D .

Finally, the influence of the number of measurements n_m on the mitigated qDD is investigated. As shown in Table 1, the value of n_m will affect the accuracy of mitigated qDD but has almost no effect on the unmitigated qDD. This can be explained by the relation between n_m and the accuracy of the distance calculation (see Fig. 7 (b)), where the mitigated distance with Richardson extrapolation is sensitive to n_m , while the unmitigated distance is almost unaffected by n_m . Since the main idea of data-driven computing is to find the material data \bar{z}_e^* closest to the admissible state \bar{z}_e , the accuracy of the calculated distance between \bar{z}_e^* and \bar{z}_e will directly influence the nearest-neighbor search, thereby affecting the performance of data-driven simulation.

In a word, error mitigation with ZNE can improve the performance of quantum computing in data-driven simulation.

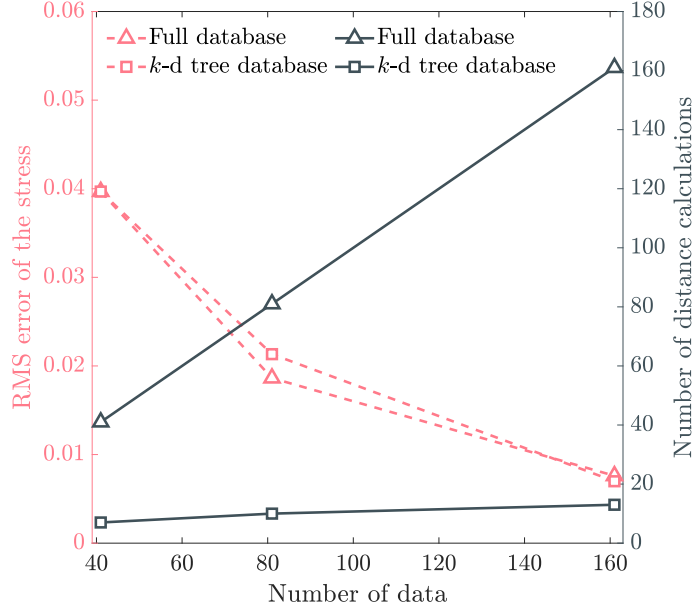


Figure 11: Performance of the k -d tree database compared with the full database.

4 Application: composite L-shaped beam

In this section, error mitigated quantum computing is applied to data-driven computational homogenization for the multiscale simulation of a composite L-shaped beam. The reference solutions are obtained by classical data-driven computational homogenization method (classical DD-FE²), which is performed on classical computers. Here, the H-based quantum algorithm with ZNE is employed to reduce the computational complexity of data-driven multiscale simulation, and it necessitates 4 qubits with a circuit depth of around 70 without folding. Meanwhile, the k -d tree data structure is also employed to reduce the number of distance calculations, resulting in a more favorable computational complexity.

The macroscopic configuration of the L-shaped beam is shown in Fig. 12, as well as the RVE at the microscopic scale. The beam is subjected to a concentrated load $F = 600$ N/mm on the right edge and a fixed constraint on the upper edge. The microstructure of the beam consists of the inclusion and the matrix, both of which are assumed to satisfy the Ramberg-Osgood constitutive relation

$$E\boldsymbol{\varepsilon} = (1 + \nu) \tilde{\boldsymbol{\sigma}} - (1 - 2\nu) p \mathbf{I} + \frac{3}{2} \alpha \left(\frac{\sigma_M}{\sigma_0} \right)^{\beta-1} \tilde{\boldsymbol{\sigma}} \quad (35)$$

where ν represents the Poisson ratio, $\tilde{\boldsymbol{\sigma}} = \boldsymbol{\sigma} + p \mathbf{I}$ denote the stress deviator, $p = -\frac{1}{3} \boldsymbol{\sigma} : \mathbf{I}$ is the equivalent hydrostatic stress, σ_M expresses the Mises equivalent stress. The material properties of the inclusion and the matrix are given in Table 2. To generate the material database, we uniformly sample the macroscopic strains in ranges $\bar{\varepsilon}_{xx} \in [-0.015, 0.030]$, $\bar{\varepsilon}_{yy} \in [-0.025, 0.040]$, and $\bar{\varepsilon}_{xy} \in [-0.015, 0.010]$. Then the macroscopic stresses are computed through computational homogenization on the RVE, resulting in 100^3 data.

For the computation at the macroscopic scale, the mitigated qDD and unmitigated qDD

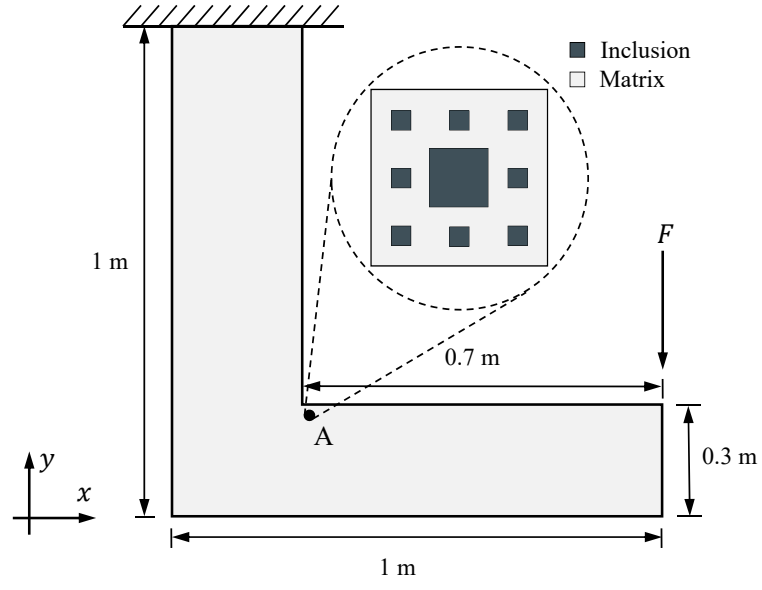


Figure 12: Sketch of the L-shaped beam.

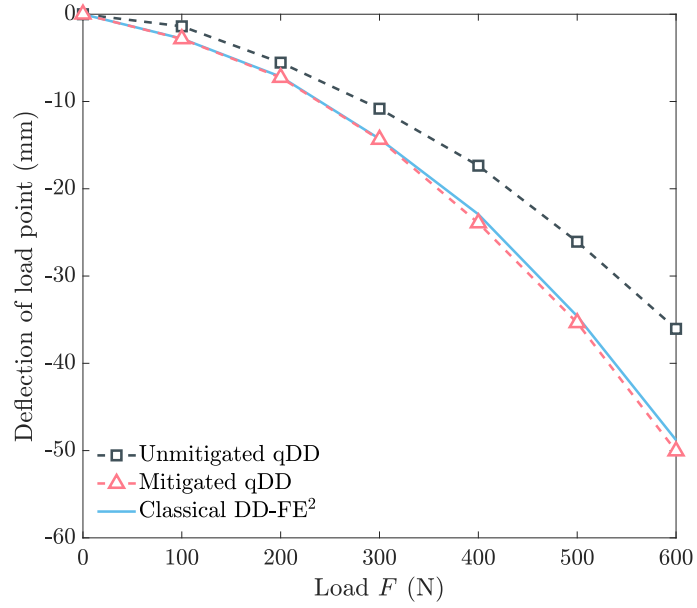


Figure 13: Deflection of the load point versus the external load.

Table 2: Material parameters of the inclusion and the matrix.

	E (MPa)	σ_0 (MPa)	ν	α	β
Inclusion	10^5	100	0.3	0.5	3
Matrix	10^4	10	0.3	0.5	3

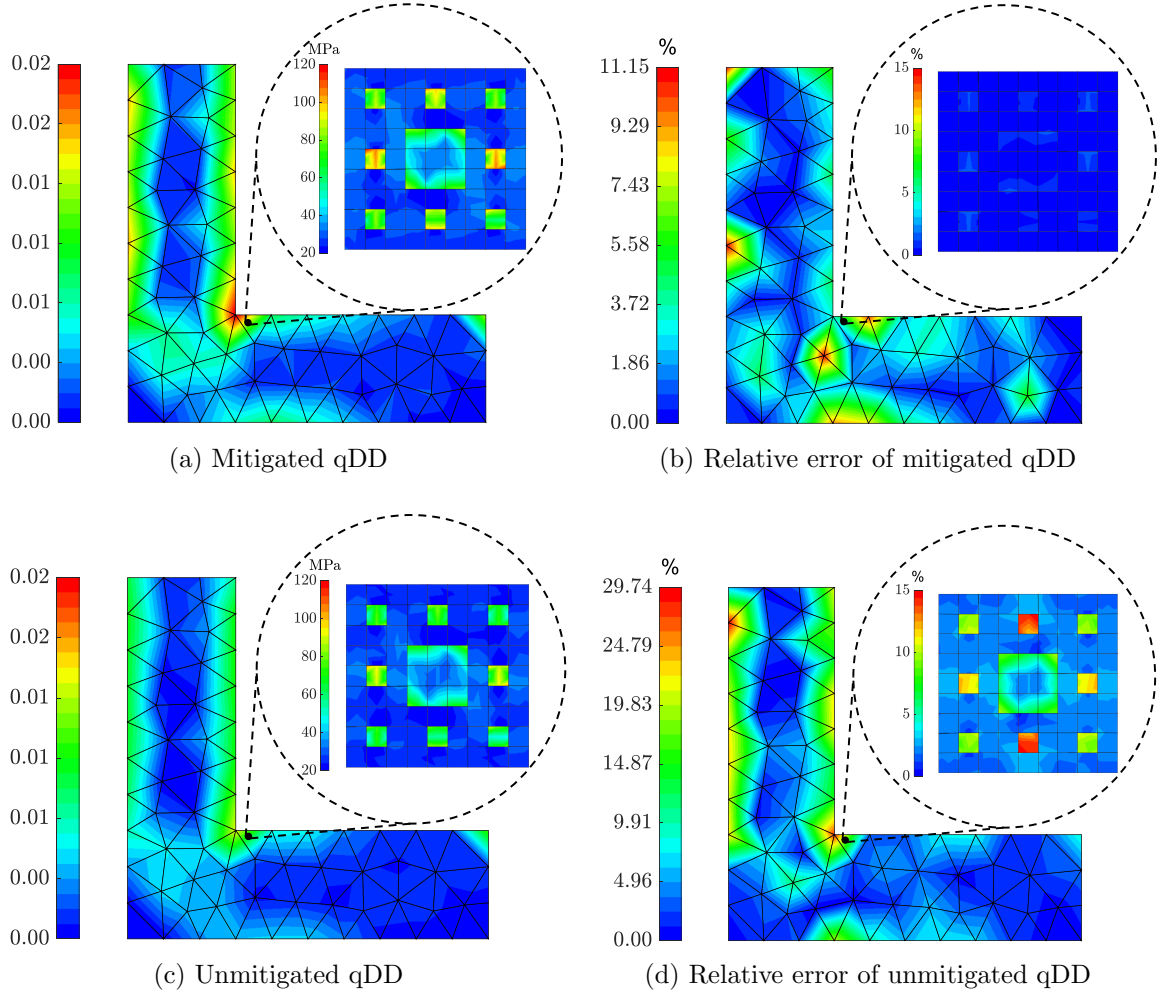


Figure 14: Strain fields $\sqrt{3J_2}$ and the corresponding relative errors for the L-shaped beam, as well as the von Mises stress fields and the corresponding relative errors for the RVE at the integration point. The solutions of classical DD-FE² are used as a reference.

are applied. As a reference, the DD-FE² method with the classical computer (referred to as classical DD-FE²) is used to solve the same problem. Fig. 13 shows the load-deflection curve of the load point. The mitigated qDD can accurately predict the deflection of the load point under various loads, while unmitigated qDD exhibits around 20% relative errors. Fig. 14 shows the strain fields $\sqrt{3J_2}$ and the corresponding relative errors at the macroscopic scale under the load $F = 600$ N/mm, as well as the von Mises stress fields and the corresponding relative errors at the microscopic scale. Compared to the unmitigated qDD, the relative error of the stress field at the microscopic scale is notably reduced, and the maximum relative error at the macroscopic scale is reduced from 29.74% to 11.15%. In a word, the mitigated qDD exhibits higher accuracy compared to the unmitigated qDD at both microscopic and macroscopic scales. This validates the effectiveness of error-mitigated quantum computing in data-driven multiscale simulation.

5 Conclusion

In realizing practical applications of quantum computing in data-driven computational homogenization, hardware noise is an unavoidable problem for NISQ quantum computers. We use zero-noise extrapolation (ZNE) to deal with this issue, which helps increase the accuracy of distance calculations and makes quantum computing perform better in data-driven computational homogenization. Two quantum algorithms for distance calculation are investigated, i.e., the Swap-based and the H-based algorithms, both of which can exponentially reduce the computational complexity. We apply ZNE in these two quantum algorithms, and the results show that the accuracy of both is improved and reaches a similar level. However, the H-based algorithm requires fewer qubits and quantum gates, exhibiting an advantage for NISQ quantum computers. Furthermore, we combine this quantum algorithm with the k -d tree data structure, making the distance calculations in data-driven computing even more efficient. Validation for a roof structure example demonstrates the effectiveness of ZNE in improving the accuracy of data-driven computing. The application to a composite L-shaped beam highlights the role of ZNE in enhancing the overall accuracy of quantum computing for data-driven computational homogenization.

We identify several directions that deserve more attention in the future. First, a real quantum computer that supports deep circuit depth is favored. After folding the gates in the circuits multiple times, the depth of the circuits may exceed the supported circuit depth of a current quantum computer. Therefore, error mitigation experiments for distance calculation on real quantum computers call for more advanced hardware devices. Second, we might explore new extrapolation methods [29, 49], or even different error mitigation techniques like probabilistic error cancellation (PEC) [26]. Thirdly, this work only demonstrates error mitigation concerning state preparation with quantum gates since qRAM is not yet available [44, 45]. The error mitigation for qRAM deserves further investigation, which could be a challenging task considering the requirements of an exponential number of ancillary qubits and long coherence time [40, 41]. Finally, the proposed method should be applied in the analysis of typical composite structures (e.g., woven fabric composites [50], rubber composites [51]) to demonstrate its performance in

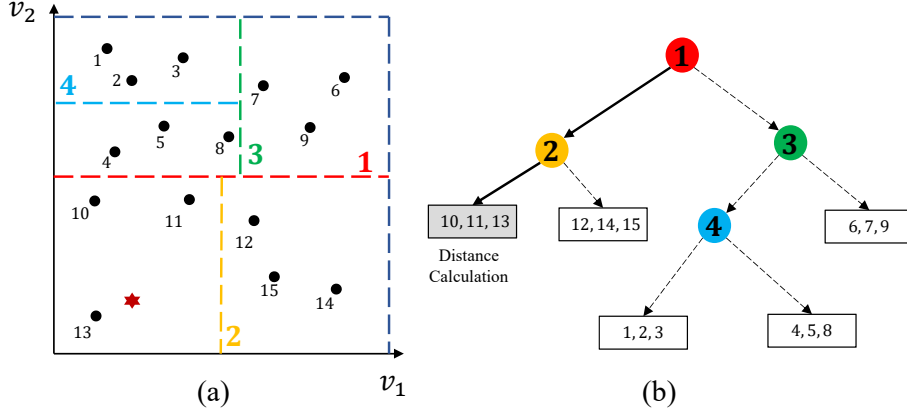


Figure 15: Diagrams of a two-dimensional k -d tree data structure. (a) Space partitioning. (b) Corresponding binary tree.

real-world engineering problems. Addressing these issues will enhance the capability of quantum computing and open an avenue for its practical application in data-driven computational homogenization.

Acknowledgements

This work has been supported by the National Key R&D Program of China (Grant No. 2022YFE0113100) and the National Natural Science Foundation of China (Grant No. 11920101002, 12172262 and 12202322).

Appendix A k -d tree data structure

The k -d tree data structure accelerates the nearest-neighbor search by reducing the number of queries. In this section, we provide a brief overview of the k -d tree data structure. For a more comprehensive understanding, interested readers can refer to [34, 36, 39] for in-depth details.

The idea behind constructing a k -d tree data structure is to partition the space using axis-aligned planes. In Fig. 15 (a), we provide an example of space partitioning for 15 data points in two dimensions. The first plane, indicated by the red dashed line labeled as ‘1’, splits the data into two subsets. This initial split serves as the root node of the data structure shown in (b). The value of v_2 for this line is determined by calculating the median of the v_2 values of all the data points. Subsequently, the resulting two subsets are further split using lines ‘2’ and ‘3’ in a similar way. The v_1 values for these lines are determined by calculating the median of the v_1 values within their respective subsets, resulting in two leaf nodes. This recursive splitting process continues until the number of data points in a subset falls below a specified threshold, which is set to 3 in this example. It is important to note that the construction of the tree structure is performed offline, thereby not adding to the computational cost during online operations.

To locate the nearest neighbor of a query data point, the search begins from the root node and proceeds down to the leaf nodes. An example query is also illustrated in Fig. 15 (a) and

(b), with the query data point denoted by the red hexagon in (a). The query route shown in (b) initiates at the root node ‘1’ and then progresses to the leaf node ‘2’. Finally, distance calculations are executed between the query data point and the data points marked as ‘10’, ‘11’, and ‘13’, resulting in the final nearest neighbor. In this work, the quantum algorithm performs distance calculations with error mitigation.

Appendix B Quantum noise model

In this paper, a noise model [33,37] is employed to approximate the hardware noise of real devices, which includes two parts:

- Single-qubit gate errors consisting of a single-qubit depolarizing error and a thermal relaxation error.
- Two-qubit gate errors consisting of a two-qubit depolarizing error followed by single qubit thermal relaxation error on each qubit participating in the gate.

Thermal relaxation is a non-unital (i.e., irreversible) process that describes the thermalization of the qubit spins towards a ground state $|0\rangle$ or an excited state $|1\rangle$. This noise model involves two different expressions which depends on the regime of relaxation time T_1 and dephasing time T_2 . For the case $T_2 \leq T_1$, the thermal relaxation model is implemented as a mixture of I , Z , reset to $|0\rangle$, reset to $|1\rangle$

$$\begin{aligned}
\rho &\longrightarrow q_{\text{id}}\rho + q_z Z\rho Z + q_{r_0} |0\rangle\langle 0|\rho|0\rangle\langle 0| + q_{r_1} |1\rangle\langle 1|\rho|1\rangle\langle 1| \\
q_{\text{id}} &= 1 - q_z - q_{r_0} - q_{r_1}, \\
q_z &= \epsilon_{T_1} \left(1 - \epsilon_{T_2} \epsilon_{T_1}^{-1}\right) / 2, \\
q_{r_0} &= (1 - q_e)(1 - \epsilon_{T_1}), \\
q_{r_1} &= q_e(1 - \epsilon_{T_1})
\end{aligned} \tag{36}$$

where $\epsilon_{T_1} = e^{-T_g/T_1}$ and $\epsilon_{T_2} = e^{-T_g/T_2}$ are respectively the probabilities for each qubit to relax and dephase after a quantum gate with evolution time T_g , q_e is related to the quantum processor’s temperature Θ , Planck’s constant h , Boltzmann’s constant k_B and frequency of the qubit f

$$q_e = \left(1 + e^{\frac{2hf}{k_B\Theta}}\right)^{-1} \tag{37}$$

Since Θ is about 15 mK, q_e is close to 0 and the error of reset to $|1\rangle$ can be omitted. Therefore,

Eq. (36) can be simplified to

$$\begin{aligned}
\rho &\longrightarrow q_{\text{id}}\rho + q_z Z\rho Z + q_{r_0} |0\rangle\langle 0| \rho |0\rangle\langle 0| \\
q_{\text{id}} &= 1 - q_z - q_{r_0} \\
q_z &= (1 - q_{r_0}) \left(1 - \epsilon_{T_2} \epsilon_{T_1}^{-1}\right) / 2 \\
q_{r_0} &= 1 - \epsilon_{T_1}
\end{aligned} \tag{38}$$

When $2T_1 > T_2 > T_1$, the thermal relaxation noise model is described by a Choi-matrix representation [33]

$$\rho \longrightarrow \text{tr}_1[\Lambda(\rho^T \otimes I)] \tag{39}$$

where tr_1 is the trace over the main system in which the density matrix ρ resides and Λ is expressed as

$$\Lambda = \begin{pmatrix} 1 - p_e p_r & 0 & 0 & \epsilon_{T_2} \\ 0 & p_e p_r & 0 & 0 \\ 0 & 0 & (1 - p_e) p_r & 0 \\ \epsilon_{T_2} & 0 & 0 & 1 - (1 - p_e) p_r \end{pmatrix} \xrightarrow{p_e \approx 0} \begin{pmatrix} 1 & 0 & 0 & \epsilon_{T_2} \\ 0 & 0 & 0 & 0 \\ 0 & 0 & p_r & 0 \\ \epsilon_{T_2} & 0 & 0 & 1 - p_r \end{pmatrix} \tag{40}$$

The depolarizing model includes a single-qubit depolarizing model and a two-qubit depolarizing model. The former is expressed as

$$\rho \longrightarrow (1 - q_1)\rho + \frac{q_1}{4} \sum_{i=0}^3 E_i \rho E_i^\dagger \tag{41}$$

while the latter is represented as

$$\rho \longrightarrow (1 - q_2)\rho + \frac{q_2}{16} \sum_{i=0}^3 \sum_{j=0}^3 E_{ij} \rho E_{ij}^\dagger, E_{ij} = E_i \otimes E_j \tag{42}$$

where E contains the identity gate I and Pauli gates $\{X, Y, Z\}$

$$E_0 = I, E_1 = X, E_2 = Y, E_3 = Z \tag{43}$$

The depolarizing probabilities q_1 and q_2 are correlated with the gate error rate ϵ_g , the relaxation error rate ϵ_{T_1} and dephasing error rate ϵ_{T_2} . Assuming that all the qubits have the same relaxation and dephasing time, then q_1 and q_2 can be expressed as

$$\begin{aligned}
q_1 &= 1 + 3 \frac{2\epsilon_g - 1}{d_1}, d_1 = \epsilon_{T_1} + 2\epsilon_{T_2} \\
q_2 &= 1 + 5 \frac{4\epsilon_g - 3}{d_2}, d_2 = 2\epsilon_{T_1} + \epsilon_{T_1}^2 + 4\epsilon_{T_2} + 4\epsilon_{T_2}^2 + 4\epsilon_{T_1} \epsilon_{T_2}
\end{aligned} \tag{44}$$

The required device data are calibrated from the IBM quantum computer *ibm_osaka* on

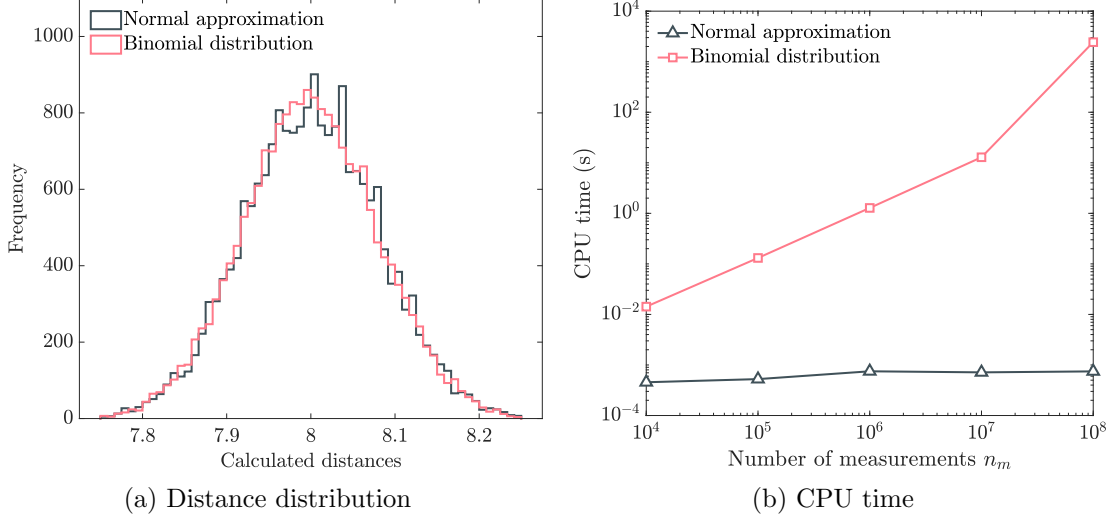


Figure 16: Performance of the normal approximation in comparison to the binomial distribution.

2024-04-15 12:15 UTC, and median values are used for noise parameters, i.e., $T_1 = 280 \mu\text{s}$, $T_2 = 127 \mu\text{s}$, gate time $T_g = 0.06 \mu\text{s}$ and error rate $\epsilon_g = 2.77 \times 10^{-4}$ for 1-qubit gates I , X and SX , gate time $T_g = 0.66 \mu\text{s}$ and error rate $\epsilon_g = 8.56 \times 10^{-3}$ for a two-qubit gate ECR .

Appendix C Normal approximation

To estimate the probability $\hat{p} = n_0/n_m$, we need to run the quantum circuit n_m times, and then get the number of $|0\rangle$ in the measurement results n_0 . This process is time-consuming when numerically conducted on a quantum computer simulator. Since one measurement relates to state $|0\rangle$ with probability p and state $|1\rangle$ with probability $1 - p$, n_0 follows a binomial distribution $n_0 \sim B(n_m, p)$. According to the central limit theorem, the distribution of n_0 becomes approximately normal with $n_0 \sim N(n_m p, n_m p(1 - p))$ if both $n_m p$ and $n_m(1 - p)$ are larger than 5. Hence, when the estimation of p is performed through a quantum computer simulator, it can be achieved by generating a random variable that obeys the corresponding normal distribution, which reduces the computational complexity of obtaining \hat{p} from $O(n_m)$ to $O(1)$.

Two numerical tests are conducted to verify the effectiveness and efficiency of the estimation method with normal approximation. Firstly, the distances between vectors $(0, 2)$ and $(2, 0)$ are calculated based on normal approximation and binomial distribution, where the number of measurements is set to $n_m = 10^5$ and 20000 samples of distances are included. As shown in Fig. 16 (a), the distance distribution obtained by normal approximation is similar to the one obtained by the binomial distribution. This means the estimation method with normal approximation retains the same statistical characteristics as the one with binomial distribution. Then, the computational times of the two estimation methods versus the number of measurements n_m are tested. As shown in Fig. 16 (b), the required computational time for normal approximation is independent of n_m , which shows its significant advantage in efficiency.

References

- [1] A. Montanaro, S. Pallister, Quantum algorithms and the finite element method, *Physical Review A* 93 (2016) 032324.
- [2] O. M. Raisuddin, S. De, FEqa: Finite element computations on quantum annealers, *Computer Methods in Applied Mechanics and Engineering* 395 (2022) 115014.
- [3] Z. Meng, Y. Yang, Quantum computing of fluid dynamics using the hydrodynamic Schrödinger equation, *Physical Review Research* 5 (2023).
- [4] B. Liu, M. Ortiz, F. Cirak, Towards quantum computational mechanics, *arXiv preprint arXiv:2312.03791* (2023).
- [5] H. Kou, Y. Zhang, H. P. Lee, Dynamic optimization based on quantum computation-a comprehensive review, *Computers & Structures* 292 (2024) 107255.
- [6] Y. Xu, J. Yang, Z. Kuang, Q. Huang, W. Huang, H. Hu, Quantum computing enhanced distance-minimizing data-driven computational mechanics, *Computer Methods in Applied Mechanics and Engineering* 419 (2024) 116675.
- [7] T. Kirchdoerfer, M. Ortiz, Data-driven computational mechanics, *Computer Methods in Applied Mechanics and Engineering* 304 (2016) 81–101.
- [8] R. Xu, J. Yang, W. Yan, Q. Huang, H. Hu, Data-driven multiscale finite element method: From concurrence to separation, *Computer Methods in Applied Mechanics and Engineering* 363 (2020) 112893.
- [9] K. Raju, T.-E. Tay, V. B. C. Tan, A review of the fe² method for composites, *Multiscale and Multidisciplinary Modeling, Experiments and Design* 4 (2021) 1–24.
- [10] W. Huang, R. Xu, J. Yang, Q. Huang, H. Hu, Data-driven multiscale simulation of FRP based on material twins, *Composite Structures* 256 (2021) 113013.
- [11] J. Yang, R. Xu, H. Hu, Q. Huang, W. Huang, Structural-Genome-Driven computing for composite structures, *Composite Structures* 215 (2019) 446–453.
- [12] Y. Xu, J. Yang, X. Bai, Q. Huang, N. Damil, H. Hu, Material database construction for data-driven computing via a continuous path-following method, *Composite Structures* (2023) 117187.
- [13] W. Yan, W. Huang, Q. Huang, J. Yang, G. Giunta, S. Belouettar, H. Hu, Data-driven multiscale method for composite plates, *Computational Mechanics* 70 (2022) 1025–1040.
- [14] S. Kim, H. Shin, Deep learning framework for multiscale finite element analysis based on data-driven mechanics and data augmentation, *Computer Methods in Applied Mechanics and Engineering* 414 (2023) 116131.

- [15] Z. Kuang, X. Bai, Q. Huang, J. Yang, W. Huang, S. Belouettar, H. Hu, Data-driven computational framework for snap-through problems, *International Journal of Solids and Structures* 269 (2023) 112226.
- [16] X. Bai, J. Yang, W. Yan, Q. Huang, S. Belouettar, H. Hu, A data-driven approach for instability analysis of thin composite structures, *Computers & Structures* 273 (2022) 106898.
- [17] K. Karapiperis, L. Stainier, M. Ortiz, J. Andrade, Data-driven multiscale modeling in mechanics, *Journal of the Mechanics and Physics of Solids* 147 (2021) 104239.
- [18] R. Eggersmann, L. Stainier, M. Ortiz, S. Reese, Efficient data structures for model-free data-driven computational mechanics, *Computer Methods in Applied Mechanics and Engineering* 382 (2021) 113855.
- [19] P. W. Shor, Fault-tolerant quantum computation, in: *Proceedings of 37th conference on foundations of computer science*, IEEE, 1996, pp. 56–65.
- [20] K. Sun, Z.-Y. Hao, Y. Wang, J.-K. Li, X.-Y. Xu, J.-S. Xu, Y.-J. Han, C.-F. Li, G.-C. Guo, Optical demonstration of quantum fault-tolerant threshold, *Light: Science & Applications* 11 (2022) 203.
- [21] M. A. Nielsen, I. L. Chuang, *Quantum Computation and Quantum Information*, 10th Edition, Cambridge University Press, USA, 2011.
- [22] National Academies of Sciences, Engineering, and Medicine, *Quantum computing: progress and prospects*, National Academies Press, 2018.
- [23] D. A. Lidar, T. A. Brun, *Quantum error correction*, Cambridge University Press, 2013.
- [24] J. Preskill, Quantum computing in the NISQ era and beyond, *Quantum* 2 (2018) 79.
- [25] S. Endo, S. C. Benjamin, Y. Li, Practical quantum error mitigation for near-future applications, *Physical Review X* 8 (2018) 031027.
- [26] K. Temme, S. Bravyi, J. M. Gambetta, Error mitigation for short-depth quantum circuits, *Physical Review Letters* 119 (2017) 180509.
- [27] Y. Li, S. C. Benjamin, Efficient variational quantum simulator incorporating active error minimization, *Physical Review X* 7 (2017) 021050.
- [28] A. Kandala, K. Temme, A. D. Córcoles, A. Mezzacapo, J. M. Chow, J. M. Gambetta, Error mitigation extends the computational reach of a noisy quantum processor, *Nature* 567 (2019) 491–495.
- [29] Y. Kim, A. Eddins, S. Anand, K. X. Wei, E. Van Den Berg, S. Rosenblatt, H. Nayfeh, Y. Wu, M. Zaletel, K. Temme, et al., Evidence for the utility of quantum computing before fault tolerance, *Nature* 618 (2023) 500–505.

- [30] D. Castelvechi, IBM quantum computer passes calculation milestone, *Nature* 618 (2023) 656–657.
- [31] S. Lloyd, M. Mohseni, P. Rebentrost, Quantum algorithms for supervised and unsupervised machine learning, *arXiv preprint arXiv:1307.0411* (2013).
- [32] S. Moradi, C. Brandner, C. Spielvogel, D. Krajnc, S. Hillmich, R. Wille, W. Drexler, L. Papp, Clinical data classification with noisy intermediate scale quantum computers, *Scientific Reports* 12 (2022) 1851.
- [33] C. Blank, D. K. Park, J.-K. K. Rhee, F. Petruccione, Quantum classifier with tailored quantum kernel, *npj Quantum Information* 6 (2020) 41.
- [34] J. H. Friedman, J. L. Bentley, R. A. Finkel, An algorithm for finding best matches in logarithmic expected time, *ACM Transactions on Mathematical Software (TOMS)* 3 (1977) 209–226.
- [35] J. Yang, X. Bai, W. Yan, W. Huang, Q. Huang, Q. Shao, H. Hu, An efficient hierarchical data searching scheme for data-driven computational mechanics, *Chinese Journal of Solid Mechanics* 42 (2021) 241–248.
- [36] B. Bahmani, W. Sun, A kd-tree-accelerated hybrid data-driven/model-based approach for poroelasticity problems with multi-fidelity multi-physics data, *Computer Methods in Applied Mechanics and Engineering* 382 (2021) 113868.
- [37] Qiskit contributors, Qiskit: An open-source framework for quantum computing (2023). [doi:10.5281/zenodo.2573505](https://doi.org/10.5281/zenodo.2573505).
- [38] Y. Hui, R. Xu, G. Giunta, G. De Pietro, H. Hu, S. Belouettar, E. Carrera, Multiscale cuf-fe2 nonlinear analysis of composite beam structures, *Computers & Structures* 221 (2019) 28–43.
- [39] T. F. Korzeniowski, K. Weinberg, A multi-level method for data-driven finite element computations, *Computer Methods in Applied Mechanics and Engineering* 379 (2021) 113740.
- [40] V. Giovannetti, S. Lloyd, L. Maccone, Quantum random access memory, *Physical Review Letters* 100 (2008) 160501.
- [41] V. Giovannetti, S. Lloyd, L. Maccone, Architectures for a quantum random access memory, *Physical Review A* 78 (2008) 052310.
- [42] H. Buhrman, R. Cleve, J. Watrous, R. De Wolf, Quantum fingerprinting, *Physical Review Letters* 87 (2001) 167902.
- [43] T. Giurgica-Tiron, Y. Hindy, R. LaRose, A. Mari, W. J. Zeng, Digital zero noise extrapolation for quantum error mitigation, in: *2020 IEEE International Conference on Quantum Computing and Engineering (QCE)*, IEEE, 2020, pp. 306–316.

- [44] S. Aaronson, Read the fine print, *Nature Physics* 11 (2015) 291–293.
- [45] J. Biamonte, P. Wittek, N. Pancotti, P. Rebentrost, N. Wiebe, S. Lloyd, Quantum machine learning, *Nature* 549 (2017) 195–202.
- [46] V. V. Shende, S. S. Bullock, I. L. Markov, Synthesis of quantum logic circuits, in: *Proceedings of the 2005 Asia and South Pacific Design Automation Conference*, 2005, pp. 272–275.
- [47] M. Krebsbach, B. Trauzettel, A. Calzona, Optimization of Richardson extrapolation for quantum error mitigation, *Physical Review A* 106 (2022) 062436.
- [48] Z. Kuang, W. Yan, K. Yu, R. Xu, L. Li, Q. Huang, J. Yang, G. Giunta, S. Belouettar, Data-driven computing for nonlinear problems of composite structures based on sub-domain search technique, *Computers & Structures* 279 (2023) 106982.
- [49] E. Van Den Berg, Z. K. Mineev, A. Kandala, K. Temme, Probabilistic error cancellation with sparse pauli–lindblad models on noisy quantum processors, *Nature Physics* (2023) 1–6.
- [50] N. Fantuzzi, M. Bacciocchi, J. Agnelli, D. Benedetti, Three-phase homogenization procedure for woven fabric composites reinforced by carbon nanotubes in thermal environment, *Composite Structures* 254 (2020) 112840.
- [51] D. Aranda-Iglesias, G. Giunta, A. Peronnet-Paquin, F. Sportelli, D. Keniray, S. Belouettar, Multiscale modelling of the mechanical response of 3D multi-axial knitted 3D spacer composites, *Composite Structures* 257 (2021) 113139.